

JGR Space Physics

RESEARCH ARTICLE

10.1029/2023JA032382

Key Points:

- Global ionospheric current system is examined by analyzing solar quiet variations of the geomagnetic field during 1–31 May 2020
- Migrating tidal components are dominant in both the Northern and Southern Hemispheres
- Eastward-propagating non-migrating tides with zonal wavenumber 1 are also detected

Correspondence to:

S. S. Chen,
sony.chen@inpe.br

Citation:

Chen, S. S., Yamazaki, Y., Denardini, C. M., Resende, L. C. A., Chagas, R. A. J., & Stolle, C. (2024). Tidal composition analysis of global Sq current system. *Journal of Geophysical Research: Space Physics*, 129, e2023JA032382. <https://doi.org/10.1029/2023JA032382>

Received 19 DEC 2023

Accepted 21 MAR 2024

Author Contributions:

Conceptualization: S. S. Chen, Y. Yamazaki

Formal analysis: S. S. Chen, Y. Yamazaki, C. M. Denardini, L. C. A. Resende, R. A. J. Chagas, C. Stolle
Investigation: S. S. Chen, Y. Yamazaki, C. M. Denardini, L. C. A. Resende, R. A. J. Chagas, C. Stolle

Methodology: S. S. Chen, Y. Yamazaki
Supervision: Y. Yamazaki,

C. M. Denardini, L. C. A. Resende

Validation: S. S. Chen, Y. Yamazaki

Visualization: S. S. Chen

Writing – original draft: S. S. Chen

Writing – review & editing: S. S. Chen, Y. Yamazaki, C. M. Denardini,

L. C. A. Resende, R. A. J. Chagas, C. Stolle

Tidal Composition Analysis of Global Sq Current System

S. S. Chen^{1,2} , Y. Yamazaki² , C. M. Denardini¹ , L. C. A. Resende^{1,3} , R. A. J. Chagas¹ , and C. Stolle² 

¹National Institute for Space Research (INPE), São José dos Campos, Brazil, ²Leibniz Institute of Atmospheric Physics at the University of Rostock (IAP), Kühlungsborn, Germany, ³State Key Laboratory of Space Weather, NSSC/CAS, Beijing, China

Abstract In this study, we examine the spatiotemporal variability of the global equivalent ionospheric current system estimated from geomagnetic Solar-quiet (Sq) variations at 124 mid- to low-latitude ground-based magnetometer stations during 1–31 May 2020. In this period, geomagnetic activity was particularly low, that is, the hourly geomagnetic activity index Hp60 did not exceed 4 σ . The spherical harmonic analysis is performed on the Sq variations to estimate the equivalent current function at each universal time hour. Hourly maps of the global Sq current system are used to evaluate, for the first time, the tidal composition of mid-latitude Sq currents and its temporal evolution. Although tides are known to be an important driver of Sq currents, the tidal composition analysis was difficult in previous studies that focused on Sq currents at particular longitude sectors. Our results show that the migrating tidal components (DW1, SW2, and TW3) are predominant in both hemispheres. This is as expected from the strong day–night contrast in ionospheric conductivities. The day-to-day variations of the migrating tidal components are, however, not strongly correlated between the two hemispheres, suggesting that these variations arise not only from the global effect of solar radiation on ionospheric conductivities but also from the local effect of neutral winds. Variations associated with non-migrating tides are also found. Especially, eastward-propagating diurnal and semidiurnal tides with zonal wavenumber 1 (DE1 and SE1) are the largest non-migrating components. Their production mechanisms remain to be understood.

1. Introduction

During geomagnetically quiet periods, ionospheric currents at 90–130 km altitude in low- to mid-latitude regions are primarily driven by the E-region dynamo. The dynamo process can be described by the ionospheric Ohm's law $\mathbf{J} = \tilde{\sigma} \cdot (\mathbf{E} + \mathbf{U} \times \mathbf{B})$, where the current density \mathbf{J} is expressed as a function of the conductivity tensor $\tilde{\sigma}$, electric field \mathbf{E} , the neutral wind \mathbf{U} and geomagnetic field \mathbf{B} . The neutral wind induces an electric field as the wind drags ions and electrons across the geomagnetic field lines in the dynamo region, where the ion-neutral collision frequencies ν_{in} are greater than the gyrofrequencies of ions Ω_i (as $\nu_{in} \gg \Omega_i$) but the electron-neutral collision frequencies ν_{en} are lower than the gyrofrequency of electrons Ω_e (as $\nu_{en} \ll \Omega_e$), resulting in the production of ionospheric dynamo currents (Maeda & Kato, 1966; Rishbeth, 1997). These currents generate a regular daily variation in the geomagnetic field, known as the solar quiet variation (Sq).

The ionospheric current system has a complex three-dimensional spatial structure (Kawano-Sasaki & Miyahara, 2008; Pfaff et al., 2020; Takeda & Maeda, 1980), which cannot be uniquely determined by ground-based Sq observations. To reduce the complexity, it is convenient to introduce the concept of the equivalent current system, in which currents flow in a spherical thin shell (Chapman & Bartels, 1940a). An effective representation of the Sq current system, for which the horizontal scale (on the order of $\sim 10^3$ km) is much larger than the vertical scale (on the order of $\sim 10^1$ km).

The equivalent Sq current system comprises external and internal parts, with the external part primarily due to ionospheric currents and the internal part generally attributed to underground currents induced by ionospheric currents (Chapman & Bartels, 1940a). The geomagnetic field variation caused by these currents can be measured using magnetometers on the ground and onboard satellites (see Yamazaki & Maute, 2017, and references therein). The spherical harmonic analysis (SHA) has been a powerful technique used to examine the equivalent Sq current system from ground and satellite geomagnetic field observations (Chapman & Bartels, 1940b; Winch, 1981; Yamazaki, 2022). Numerous studies have been conducted to analyze the features of the equivalent Sq current system, such as the strength and central position of the Sq current whorl (e.g., Liu et al., 2021; Stening & Winch, 2013; Takeda, 2002; Yamazaki, Yumoto, Cardinal, et al., 2011, and others).

The dynamo-region currents can be modulated by atmospheric oscillations such as the tides caused by the absorption of solar radiation in the lower atmosphere, which propagate to the mesosphere-lower-thermosphere (MLT) region (Richmond, 1979). Following Forbes et al. (2008), tidal oscillations in the Earth's atmosphere can be expressed by $A_{n,s} \cos(n\Omega t + s\lambda - \phi_{n,s})$, where $A_{n,s}$ and $\phi_{n,s}$ denote the amplitude and phase of the oscillation for each n th ($=1, 2, 3, \dots$) harmonic of the solar-day oscillation and zonal wavenumber s ($=\dots, -3, -2, -1, 0, 1, 2, 3, \dots$), respectively. Ω , t , and λ denote the rotation rate of the Earth ($2\pi/\text{day}$), the time (days), and the longitude (radians), respectively. The westward (eastward) propagating wave components are denoted by $s > 0$ ($s < 0$), whereas the zonally symmetric oscillation is denoted by $s = 0$. The tides with $n = s$ propagate westward with the apparent motion of the Sun, and are called migrating tides. All the other tides ($n \neq s$) are called non-migrating tides.

Various modes of tides are found in the dynamo region (Forbes et al., 2008; Oberheide et al., 2011; Truskowski et al., 2014; Yamazaki et al., 2023), and some of these tides are known to be important for driving ionospheric currents. Early modeling studies have shown that the global feature of the ionospheric current system can be reproduced by driving a dynamo model with the neutral wind associated with the migrating diurnal and semi-diurnal tides (Forbes & Lindzen, 1976; Richmond et al., 1976; Stening, 1977; Tarpley, 1970). Although previous studies have established that not only migrating but also non-migrating tidal components are important for the equatorial electrojet (EEJ) (Lühr & Manoj, 2013; Soares et al., 2022), the tidal composition of mid-latitude Sq currents have not been examined, as most previous studies focused on Sq currents at particular longitude sectors.

In this study, we examine the global equivalent Sq current system using the SHA of ground-based magnetometer data in May 2020 to investigate the temporal and spatial variations of the Sq current system and discuss their implications. We evaluate the temporal (day-to-day) evolution of different tidal components in the northern and southern Sq current intensities for the first time.

2. Data Selection and Methods

We estimate the equivalent Sq current system using ground-based magnetometer data from a total of 124 stations. The stations are located between $\pm 60^\circ$ latitude regions in the quasi-dipole magnetic coordinate system (Emmert et al., 2010). In the remainder of the paper, the quasi-dipole latitude and longitude are abbreviated as QLAT and QLon, respectively. We obtain the magnetic data from several sources, including SuperMAG (Gjerloev, 2012), INTERMAGNET (Love, 2008), Embrace MagNet (Denardini et al., 2018), and LISN/IGP (Valladares & Chau, 2012), which provide 110, 4, 8, and 2 magnetometer stations, respectively. Our analysis includes 85 mid-latitude stations ($30^\circ\text{--}60^\circ\text{N}$ and $30^\circ\text{--}60^\circ\text{S}$ QLAT), 36 low-latitude stations ($5^\circ\text{--}30^\circ\text{N}$ and $5^\circ\text{--}30^\circ\text{S}$ QLAT), and three equatorial stations ($5^\circ\text{N--}5^\circ\text{S}$ QLAT).

The selected time period (1–31 May 2020) corresponds to very low geomagnetic activity. It contains 17 consecutive days when the daily maximum value of the Hp60 index did not exceed 3σ . Hp60 is a geomagnetic activity index described by Yamazaki et al. (2022). It has effectively the same occurrence distribution as the Kp index (Matzka et al., 2021) but has the higher time resolution of 1 hr in contrast to 3 hr for Kp . The Hp60 value did not exceed 4σ during the whole period.

Figure 1 displays the ground-based stations we selected around the globe at 15:30 universal time (UT) on 1 May 2020. The red and black lines represent the magnetic equator and $\pm 60^\circ$ QLAT, respectively. The background color represents the total magnetic field intensity obtained from the IGRF-13 model (Alken et al., 2021), and the night side is shown in a darker color. The ground-based stations are selected between $\pm 60^\circ$ QLAT to avoid the disturbance magnetic field from the high-latitude current system (Laundal et al., 2018). Additionally, the polar view maps are provided in the top-left and top-right corners of the figure.

The magnetic data obtained in the geographic coordinates (GEO) were processed as described below, and Sq variations were derived in the local magnetic coordinates (MAG). We define the GEO coordinates as follows: its X -axis points toward the geographic North, its Y -axis points toward the geographic East, and its Z -axis points to the center of Earth. On the other hand, the MAG coordinates has its X , Y , and Z axes pointing toward the local magnetic North, local magnetic East, and downward directions, respectively. First, we re-sampled 1-min magnetic data to 1-hr by averaging the data at each UT hour over 60 min centered at minute 30 (e.g., averaging 00:00–00:59 UT yields a value at 00:30 UT). The retrieval procedures for the Sq variation are described below, and are

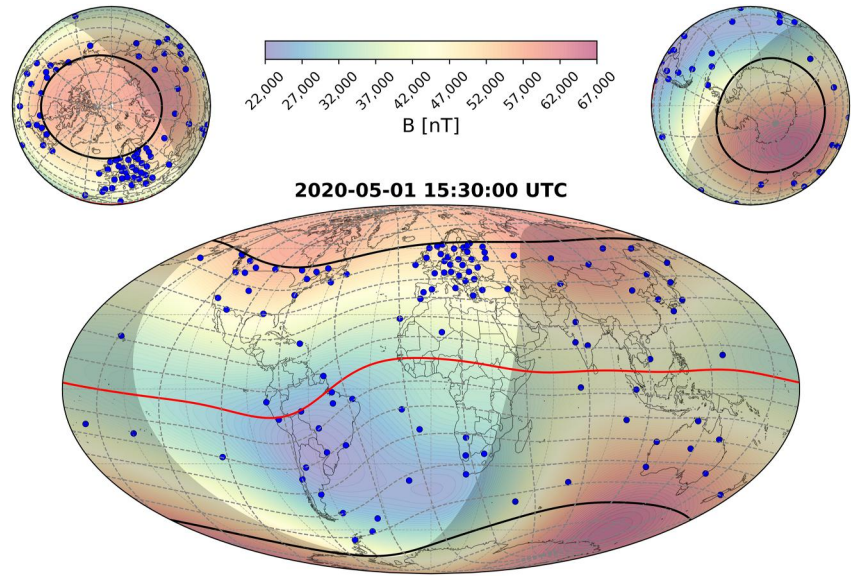


Figure 1. Selected stations around the globe on 1 May 2020, at 15:30 universal time. The magnetic equator and $\pm 60^\circ$ quasi-dipole latitude are shown in red and black lines, respectively. The background color indicates the total magnetic field intensity from IGRF-13 model and the night side is shown in a darker color.

also demonstrated in Figure 2 using the magnetic northward component (ΔN) of the geomagnetic field observed at the Niemegk observatory (NGK, 52.07°N , 12.68°E) as an example.

1. The geomagnetic field variation represented in GEO coordinates ($\mathbf{B}_{\text{GEO}}^{\text{OBS}}$; Figure 2, top panel, black line) is obtained by subtracting the monthly median from the raw data. This is done for each vector component of the geomagnetic field (i.e., X , Y , and Z) to determine the observed magnetic field variations.
2. The geomagnetic field variation is also obtained using CHAOS-7 ($\mathbf{B}_{\text{GEO}}^{\text{CHAOS7}}$; Figure 2, top panel, red line). CHAOS-7 (Finlay et al., 2020; Olsen et al., 2006) is an empirical model of the geomagnetic field. It can predict the main field, lithosphere field, and magnetospheric field for a given location and time. We subtract the monthly median value from each orthogonal component of the CHAOS-7 model output to get the $\mathbf{B}_{\text{GEO}}^{\text{CHAOS7}}$. It may be noted in Figure 2 (top panel, red line) that $\mathbf{B}_{\text{GEO}}^{\text{CHAOS7}}$ exhibits daily variation. The daily variation in $\mathbf{B}_{\text{GEO}}^{\text{CHAOS7}}$ is not due to Sq currents but due to large-scale magnetospheric currents (Lühr et al., 2017), which needs to be removed from the magnetic data for studying Sq.
3. The residual magnetic field ($\delta\mathbf{B}_{\text{GEO}}$; Figure 2, middle panel, blue line) is obtained after subtracting the CHAOS-7 model output from the observation for each orthogonal component of the geomagnetic field (i.e., δX , δY , and δZ), as shown in Equation 1:

$$\delta\mathbf{B}_{\text{GEO}} = \mathbf{B}_{\text{GEO}}^{\text{OBS}} - \mathbf{B}_{\text{GEO}}^{\text{CHAOS7}}. \quad (1)$$

4. The magnetic field baseline during quiet geomagnetic activity ($\delta\mathbf{B}_{\text{GEO}}^{\text{baseline}}$; Figure 2, middle panel, red line) is obtained from the residual magnetic field. The baseline is the linear regression of the residual magnetic field at local midnight when the Hp60 index did not exceed 2– (Figure 2, middle panel, blue dots). In other words, we assume the currents to be vanishingly small (i.e., small in an absolute sense) at local midnight.
5. The Sq variation in the GEO ($\Delta\mathbf{B}_{\text{GEO}}$; Figure 2, bottom panel, black line) is obtained after subtracting the baseline from the residual magnetic field, as shown in Equation 2:

$$\Delta\mathbf{B}_{\text{GEO}} = \delta\mathbf{B}_{\text{GEO}} - \delta\mathbf{B}_{\text{GEO}}^{\text{baseline}} \equiv \begin{bmatrix} \Delta X \\ \Delta Y \\ \Delta Z \end{bmatrix}, \quad (2)$$

where ΔX , ΔY , and ΔZ are the components of the Sq variation represented in GEO coordinates (in nT).

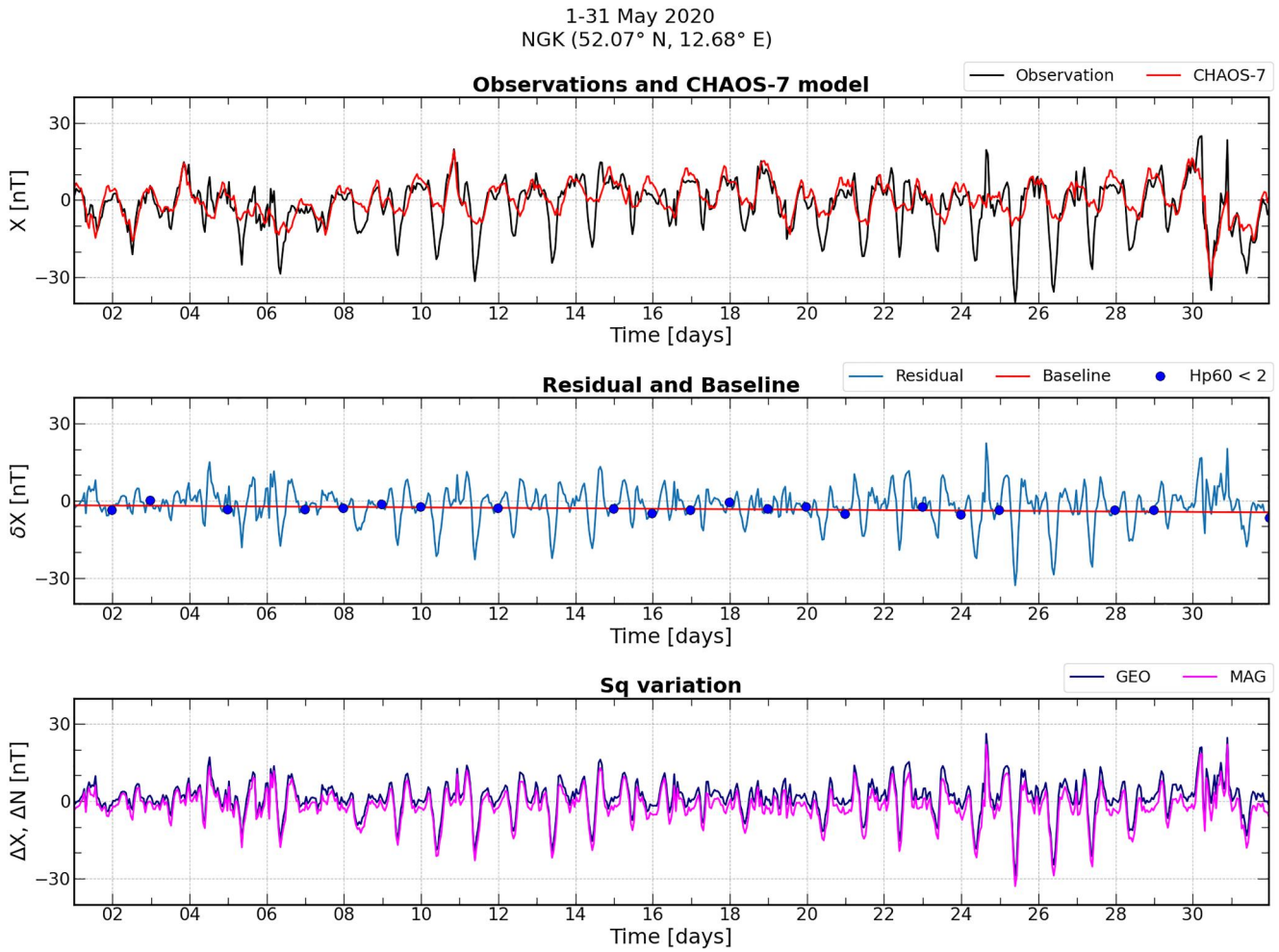


Figure 2. Illustration of the data preprocessing used to obtain the northward component of the solar quiet (Sq) variation in the local magnetic coordinate (ΔN) at Niemegek (NGK, 52.07°N, 12.68°E) during 1–31 May 2020. The top panel shows the geomagnetic field variation in the north component (X) from ground-based observations (black line) and the CHAOS-7 model output (red line). The middle panel shows the residual magnetic field (blue line, δX), the magnetic field baseline during quiet-time geomagnetic activity (red line), and the residual magnetic field at local midnight when $H_p60 < 2$ (blue dots). The bottom panel shows the northward component of the Sq variation in geographic (navy, ΔX) and local magnetic (magenta, ΔN) coordinates.

6. A vector represented in the GEO coordinates can be transformed to the local MAG ($\Delta \mathbf{B}_{\text{MAG}}$; Figure 2, bottom panel, magenta line) by rotating GEO by the angle of local magnetic declination about its Z-axis, as shown in Equation 3:

$$\Delta \mathbf{B}_{\text{MAG}} \equiv \begin{bmatrix} \Delta N \\ \Delta E \\ \Delta Z \end{bmatrix} = \begin{bmatrix} \cos D & \sin D & 0 \\ -\sin D & \cos D & 0 \\ 0 & 0 & 1 \end{bmatrix} \begin{bmatrix} \Delta X \\ \Delta Y \\ \Delta Z \end{bmatrix}, \quad (3)$$

where ΔN , ΔE , and ΔZ are the components of the Sq variation represented in MAG coordinates (in nT). D is the local magnetic declination angle obtained with the IGRF-13 model.

2.1. Spherical Harmonic Analysis

We conducted a SHA on the Sq variation to estimate the global ionospheric current system. The method we used is based on the approach developed by Suzuki (1978) but with some modifications. Suzuki (1978) performed the

SHA to the Sq data from a non-uniform and sparse distribution of stations between $\pm 60^\circ$ in geomagnetic latitude. Important features of his method for analyzing the geomagnetic Sq field are as follows: (a) exclusion of equatorial stations, (b) simultaneous use of the three orthogonal components of the geomagnetic field, (c) adoption of a weight function for each station, and (d) creation of some ghost stations. Below we explain our SHA technique highlighting the difference from Suzuki (1978).

We start with the creation of ghost station data. Ghost stations are virtual stations deployed in regions of sparse observations. Suzuki (1978) used eight ghost stations, for which Sq variations were estimated using magnetic data from other (real) stations. In this study, we created five ghost stations in the nightside low-latitude region, where Sq dynamo currents are expected to be negligibly small. Their geographical locations change over time so that they will always stay in the nightside. This contrasts with the ghost stations used by Suzuki (1978), whose geographical locations were fixed. One of the five ghost stations are located where the solar zenith angle is 180° (i.e., the local midnight), and the four other stations are located at $\pm 30^\circ$ latitude and longitudes from that point. We set all the Sq components (i.e., ΔN , ΔE , and ΔZ) to 0 nT at the ghost stations. This assures the presence of Sq data in the nighttime sector and helps to avoid overfitting in the SHA, which will be described later. Similarly, ΔN , ΔE , and ΔZ were also set to 0 nT at the magnetic poles.

We performed the averaging of ΔN , ΔE , and ΔZ in each latitude-longitude grid of $5^\circ \times 5^\circ$ at each UT hour. This is to avoid the over-representation of the Sq data from stations in densely-distributed regions like Europe.

The ΔN and ΔZ components from the stations near the magnetic equator, that is, within $\pm 5^\circ$ QLAT, were excluded from further analysis to prevent contamination from the EEJ. Unlike Suzuki (1978), ΔE from the equatorial stations are kept in our SHA. Ground magnetic signatures of the EEJ can be found in the N and Z components observed near the magnetic equator (Doumouya et al., 2003; Rastogi, 1989; Rigoti et al., 1999). The localized geomagnetic perturbations due to the EEJ cannot be resolved by the low-degree spherical harmonics that are employed in our SHA for Sq.

The obtained three orthogonal components of the Sq field (ΔN , ΔE , and ΔZ) were used in the SHA. Although, strictly speaking, N and E are not in the same direction as the magnetic north and east in the quasi-dipole coordinate system, we ignore the misalignment between the quasi-dipole and local MAG in the present study.

Also, we truncated the spherical harmonic expansion performed on the Sq variation at the fourth harmonic degree ($N = 4$). This degree is known to be sufficient for capturing the global feature of the Sq current system, as reported by Takeda (2002). The harmonic analysis allowed us to determine the magnetic potential V , as described by Yamazaki and Maute (2017):

$$V = R_E \sum_{n=1}^N \left[\left(\frac{r}{R_E} \right)^n \sum_{m=0}^n \{ g_{ex_n}^m \cos(m\phi) + h_{ex_n}^m \sin(m\phi) \} P_n^m(\cos \theta) \right] + R_E \sum_{n=1}^N \left[\left(\frac{R_E}{r} \right)^{n+1} \sum_{m=0}^n \{ g_{in_n}^m \cos(m\phi) + h_{in_n}^m \sin(m\phi) \} P_n^m(\cos \theta) \right] + C, \quad (4)$$

where V denotes the magnetic potential, C denotes an arbitrary constant, r is the sphere shell radius (that is, $r = R_E + h$), R_E is the Earth's radii ($=6,371.2$ km), and h is the height of the ionospheric current at E region ($=110$ km). θ and ϕ are colatitudes and longitudes in quasi-dipole coordinates, respectively. $P_n^m(\cos \theta)$ is the quasi-normalized Legendre polynomials for n th degree and m th order. The so-called Gauss coefficients $g_{ex_n}^m$ and $h_{ex_n}^m$ refer to the parts of external origin (in nT) and $g_{in_n}^m$ and $h_{in_n}^m$ refer to the parts of internal origin (in nT), both for n th degree and m th order. From the magnetic potential, the orthogonal components of the Sq field are determined as (Chapman & Bartels, 1940b; Yamazaki & Maute, 2017):

$$\Delta N = \sum_{n=1}^N \sum_{m=0}^n \left[\frac{dP_n^m(\cos \theta)}{d\theta} \cos(m\phi) \right] (g_{ex_n}^m + g_{in_n}^m) + \sum_{n=1}^N \sum_{m=0}^n \left[\frac{dP_n^m(\cos \theta)}{d\theta} \sin(m\phi) \right] (h_{ex_n}^m + h_{in_n}^m), \quad (5)$$

$$\Delta E = \sum_{n=1}^N \sum_{m=0}^n \left[\frac{m}{\sin \theta} P_n^m(\cos \theta) \sin(m\phi) \right] (g_{ex_n}^m + g_{in_n}^m) - \sum_{n=1}^N \sum_{m=0}^n \left[\frac{m}{\sin \theta} P_n^m(\cos \theta) \cos(m\phi) \right] (h_{ex_n}^m + h_{in_n}^m), \quad (6)$$

$$\Delta Z = \sum_{n=1}^N \sum_{m=0}^n [P_n^m(\cos \theta) \cos(m\phi)] [n g_{ex_n}^m - (n+1) g_{in_n}^m] + \sum_{n=1}^N \sum_{m=0}^n [P_n^m(\cos \theta) \sin(m\phi)] [n h_{ex_n}^m - (n+1) h_{in_n}^m], \quad (7)$$

where ΔN , ΔE , and ΔZ are the Sq field in the local magnetic north, local magnetic east, and downward magnetic field components (in nT), respectively. The *Gauss coefficients* were determined based on the least squares fitting method so that the difference between the Sq variation and Equations 5–7 will be the smallest.

For the present study, only the external part of the equivalent Sq current system is examined. The current function (in units of amperes) for the external equivalent Sq current system is given as follows (Chapman & Bartels, 1940b; Yamazaki, 2022):

$$J_{ex} = R_E \sum_{n=1}^N \left[-\frac{10}{4\pi} \frac{2n+1}{n+1} \left(\frac{r}{R_E} \right)^n \sum_{m=0}^n \{ g_{ex_n}^m \cos(m\phi) + h_{ex_n}^m \sin(m\phi) \} P_n^m(\cos \theta) \right], \quad (8)$$

where J_{ex} is the external part of the equivalent current function.

2.2. Tidal Composition Analysis

We performed Fourier-wavelet analysis to identify global-scale wave activity in the equivalent current function. The Fourier-wavelet analysis is a spectral method developed by Yamazaki (2023), which provides amplitude spectra of eastward- and westward-propagating waves with different zonal wavenumbers. The Python code that we used in this study is available at <https://git.iap-kborn.de/yamazaki/fourierwavelet>. The method involves the Fast-Fourier Transform (Frigo & Johnson, 1998) in longitude, followed by the wavelet transform (Torrence & Compo, 1998) in time. In our case, the input data is a 2-D matrix of the equivalent current function as a function of magnetic longitude and time, sampled at the magnetic latitudes of the Sq foci. The amplitude spectra for zonal wavenumbers 1, 2, and 3 were examined.

3. Results and Discussions

3.1. Features of the Global Equivalent Sq Current System

The external part of the global equivalent Sq current system was determined for each UT hour during 1–31 May 2020 using the SHA. Figure 3 shows contour plots of the equivalent Sq current function at various universal times on 4 May 2020. Each panel shows the map of the global equivalent Sq current function in quasi-dipole coordinates at 00:30 UT, 04:30 UT, 08:30 UT, 12:30 UT, 16:30 UT, and 20:30 UT, from top to bottom. The red-blue color scale indicates positive (solid line) and negative (dashed lines) values of the current function in kilo-amperes with isolines contours every 30 kA. Magnetic stations are marked with black dots, and the magnetic equator is represented by the red line. The plus-red and minus-blue symbols indicate the Sq foci in the Northern and Southern Hemisphere, respectively, marked with their peak value. The corresponding Hp60 geomagnetic activity index is shown at the top of each map. This figure illustrates the spatiotemporal variability of the equivalent ionospheric current intensity, regardless of the low geomagnetic activity level shown in the Hp60 index.

At each UT, the local maximum (in the Northern Hemisphere) and minimum (in the Southern Hemisphere) of the Sq current function are identified as Sq foci. They correspond to the central position of the Sq current whorl in the Northern and Southern Hemispheres (e.g., Hasegawa, 1960). Figure 4 depicts the temporal variability of the following three parameters during 1–31 May 2020: (a) the absolute values of the Sq current function at the Sq foci, which represent the total amount of Sq currents flowing in each hemisphere, (b) the QLAT of the Sq foci, and

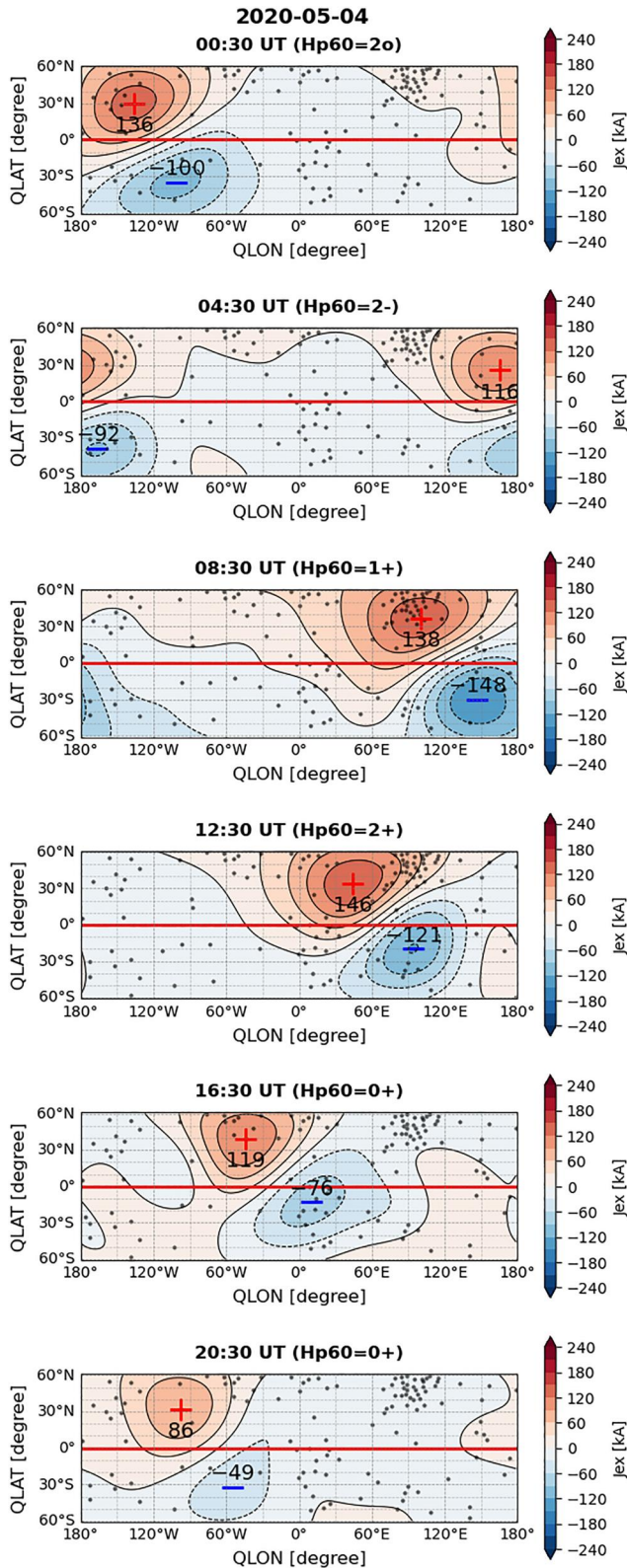


Figure 3.

(c) the longitudinal displacement of the Sq foci from the noon meridian. The background color corresponds to the hourly geomagnetic activity index Hp60 from 0o to 4o. During 91.67% of the period, the Hp60 index varied between 0o and 2o, indicating a geomagnetically quiet period in May 2020. In Figure 4, gaps are occasionally seen in the data. This is because Sq foci are sometimes not detectable, especially during periods of relatively high geomagnetic activity. The disappearance of Sq foci during high geomagnetic activity was also noted in previous studies (e.g., Yamazaki et al., 2016).

In Figure 4a, the current intensity is relatively higher in the Northern Hemisphere than in the Southern Hemisphere, with the mean value and its corresponding standard deviation of 145 ± 32 and 84 ± 24 kA, respectively. This observation aligns with previous studies, which consistently note stronger Sq current intensity in the Northern Hemisphere during May (Owolabi et al., 2022; Takeda, 2002; Yamazaki, Yumoto, Cardinal, et al., 2011). Hibberd and Davidson (1988) reported that the Sq current intensities in the Northern and Southern Hemispheres tend to vary similarly. However, we identified a weak positive correlation ($r = 0.33$) between the northern and southern Sq current intensities in our analysis. Day-to-day variability in the Sq current intensity is seen in both hemispheres. Yamazaki et al. (2016) numerically demonstrated that the day-to-day variability in the Sq current intensity can be largely attributed to the effect of atmospheric waves that propagate from the troposphere and stratosphere (below 30 km).

Moreover, we found a positive trend of 1.3 kA/day in the northern Sq current intensity and a negative trend of -1.0 kA/day in the southern Sq current intensity during May 2020. These observed trends in intensities align with the well-documented seasonal variations of the Sq currents. Prior studies have consistently shown that the northern Sq currents tends to increase while the southern Sq current intensity tends to decrease from the March equinox to the June solstice (e.g., Owolabi et al., 2022; Yamazaki, Yumoto, Cardinal, et al., 2011).

Upon comparing the geomagnetic activity with the Sq current intensity, we observed a tendency for the strength of the Sq current to decrease following enhanced geomagnetic activity (i.e., Hp60 is between 2o and 4o) in both the Northern and Southern Hemispheres. This reduction is evident on days 1, 4–6, 10–11, 19, 22, 25, and 31. To investigate this characteristic, we analyzed the correlation between the hourly Sq current intensities and Hp60. The monthly-mean UT variation of the Sq current intensity was determined and removed from the time series of the Sq current intensity in each hemisphere. The residual Sq current intensities were compared with Hp60 considering time lags. The results revealed the absence of correlation at zero lag, while a weak but statistically significant negative correlation ($r \approx -0.2$, $p < 0.05$) emerged

Figure 3. Contour plots of the external part of the global equivalent solar quiet (Sq) currents system intensity on 4 May 2020, at 00:30 universal time (UT), 04:30 UT, 08:30 UT, 12:30 UT, 18:30 UT, and 20:30 UT, from top to bottom panels, respectively. The vertical and horizontal axes correspond to the latitude and longitude in quasi-dipole coordinates, respectively. The red-blue color scale indicates positive (solid line) and negative (dashed lines) values of the current function in kilo-amperes with isolines contours every 30 kA. The black dots indicate the magnetic station and the red line is the magnetic equator. The plus-red and minus-blue symbols indicate the Sq foci in the Northern and Southern Hemisphere, respectively, marked with their peak value. The corresponding Hp60 geomagnetic activity index is shown at the top of each map.

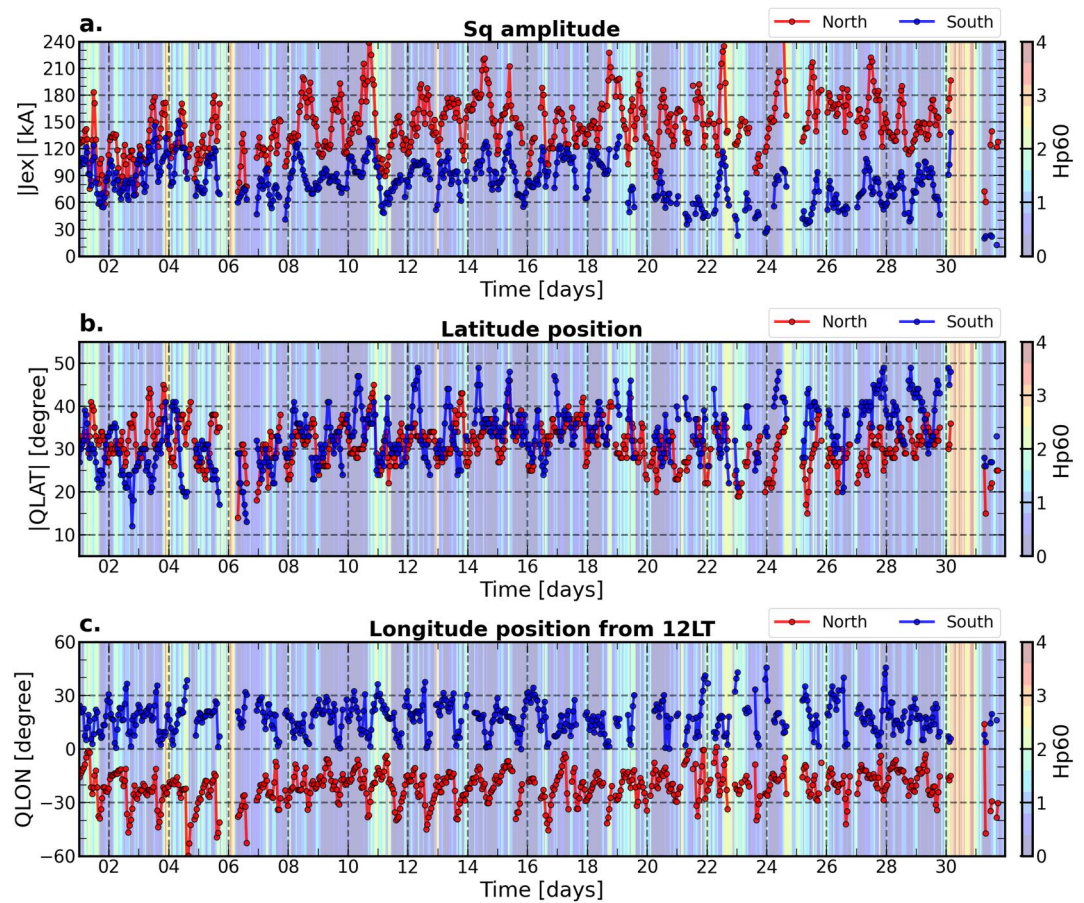


Figure 4. Time series of the (a) the absolute value of the solar quiet (Sq) current intensity, (b) the absolute value of Sq foci QLAT, and (c) the longitudinal distance between the noon meridian and Sq foci, both in the Northern (red circle) and Southern (blue circle) Hemispheres during 1–31 May 2020. The background color corresponds to the hourly geomagnetic activity index Hp60 from 0 to 4.

when the Sq current intensities were lagged behind Hp60 by 3–6 hr. This means that there is a time delay of several hours for the Sq current intensity to respond to enhanced geomagnetic activity. The negative response of Sq current intensities to Hp60 is likely due to the disturbance dynamo effect (Blanc & Richmond, 1980), which was also reported in previous observational studies (Le Huy & Amory-Mazaudier, 2008; Yamazaki, Yumoto, Uozumi, & Cardinal, 2011).

In Figure 4b, the mean value of the Sq focus latitude and its corresponding standard deviation in the Northern Hemisphere is $31^{\circ} \pm 5^{\circ}$ QLAT, while in the Southern Hemisphere, it is $-33^{\circ} \pm 7^{\circ}$ QLAT. This aligns with findings by Campbell and Schiffmacher (1985), Campbell and Schiffmacher (1988), who reported that the Sq focus latitude ranges from 30° to 42.5° magnetic latitude in the Northern Hemisphere and -35.0° to -22.5° magnetic latitude in the Southern Hemisphere in May. Previous studies have shown an equatorward shift of the Sq foci with increasing Sq current intensities (Kane, 1974; Takeda, 1999). We noted a poleward shift of the southern Sq focus by approximately 10° starting from day 19, coinciding with a reduction in the strength of the southern Sq current intensity. The previous study by Stening et al. (2005) reported a poleward shift of the Sq foci with increasing strength of the EEJ. However, the EEJ is not evaluated in this study. The day-to-day relationship between the Sq focus latitude and Sq intensity is not clear in our data. Additionally, we observed a shift of the Sq foci toward the equator (pole) with increasing (decreasing) geomagnetic activity in both the Northern and Southern Hemispheres. Nevertheless, further studies may be conducted to investigate the physical mechanism of the systematic scattering of the Sq foci with geomagnetic activity.

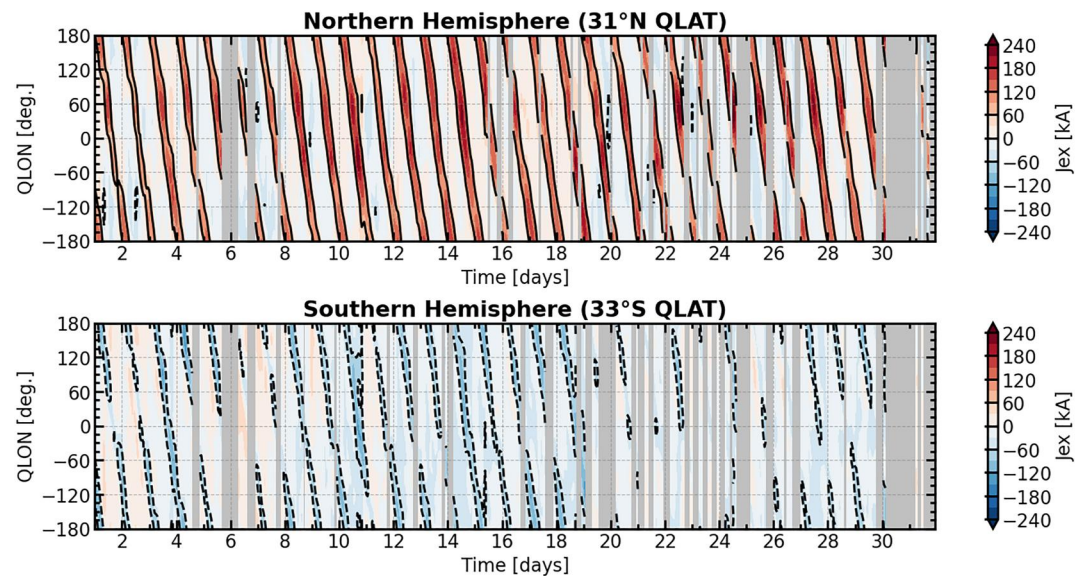


Figure 5. The contour plots of the solar quiet (Sq) current system intensity as a function of quasi-dipole longitude and each universal time hour on 1–31 May 2020 in the Northern (31°N QLAT, top panel) and Southern (33°S QLAT, bottom panel) Hemispheres. The black solid and dashed lines indicate the Sq intensity of 60 and –60 kA, respectively. The gray shading corresponds to the time when Sq foci are not determined.

The longitudinal distance between the noon meridian and Sq foci is depicted in the bottom panel (Figure 4c). As shown in this panel, the northern Sq focus is shifted to the morning sector and the southern Sq focus is shifted to the afternoon sector at all UTs, which is also seen in Figure 3. On average, the northern Sq focus is located approximately 30° west of the southern Sq focus. In other words, the northern Sq focus appears earlier than the southern Sq focus by approximately 2 hours in local time. The results are consistent with findings from previous climatological studies (e.g., Campbell & Schiffmacher, 1985, 1988; Liu et al., 2024; Yamazaki, Yumoto, Cardinal, et al., 2011). However, our investigation explores novel aspects of the global Sq external current function in a continuous quiet days, capturing the day-to-day and longitudinal variation of both the northern and southern Sq current whorls at different UT times.

Longitudinal (and hence UT) variation of the Sq current system can result from various causes. One important factor is the longitudinal variation of the main geomagnetic field intensity. Since ionospheric conductivities depend on the intensity of the main geomagnetic field, the longitudinal variation of the main geomagnetic field leads to the longitudinal variation of Sq currents (Stening, 1971). Another factor to be considered is non-migrating tides. Unlike migrating tides, neutral wind perturbations due to non-migrating tides vary with longitude at a fixed local time. This can lead to the longitudinal variation in the $\mathbf{U} \times \mathbf{B}$ electromotive force and thus Sq currents. Previous studies based on global satellite magnetic measurements found some hint of non-migrating tidal effects on the Sq current system (e.g., Chulliat et al., 2016; Pedatella et al., 2011).

Figure 5 displays the Sq current intensities at 31°N QLAT (top panel) and 33°S QLAT (bottom panel) as a function of magnetic longitude and time during May 2020. These latitudes correspond to the monthly mean values of the Sq focus latitudes. The contours indicated as black solid and dashed lines are the Sq current intensity of 60 kA and –60 kA, respectively. The gray shading corresponds to the time when Sq foci are not determined. In the Northern Hemisphere, the Sq current intensity at the magnetic latitude of the Sq focus position exhibits consistent variations. The Sq current intensity in the Southern Hemisphere exhibits more pronounced UT (day-to-day and hour-to-hour) and longitude variabilities.

3.2. The Tidal Variability in the Sq Current Intensity

The Fourier-wavelet analysis (Yamazaki, 2023) was performed on the longitude-time data of the Sq current intensities presented in Figure 5. Figure 6 shows the amplitude spectra for the westward-propagating components with zonal wavenumbers 1, 2, and 3 (W1, W2, and W3, respectively) at the northern (left panels) and southern

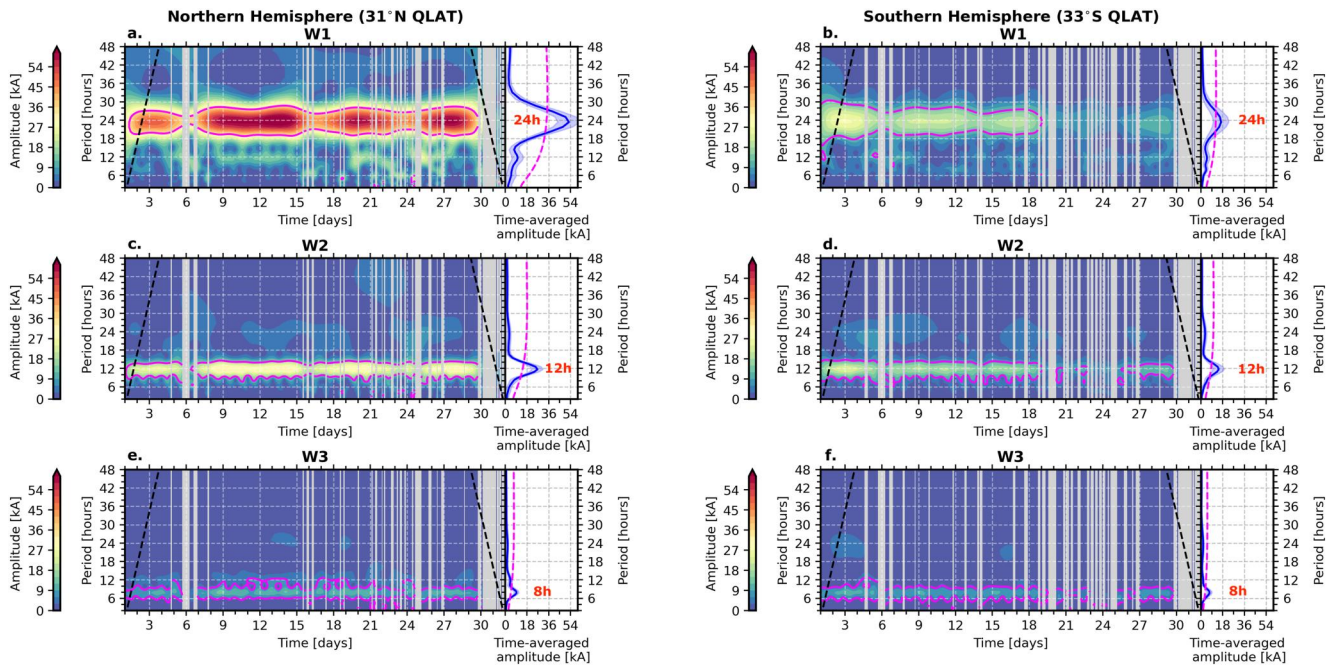


Figure 6. Fourier-wavelet spectra for the solar quiet (Sq) current intensity at the Sq focus latitudes in the Northern Hemisphere (a, c, e) and Southern Hemisphere (b, d, f) during 1–31 May 2020, for the westward-propagating components with zonal wavenumbers 1, 2, and 3 (W1, W2, and W3, respectively). Magenta lines correspond to the amplitude at the 95% confidence level. The gray shading indicates the time when Sq foci were noted determined. The time-averaged amplitude (blue line) is also shown next to each panel.

(right panels) Sq foci. The W1 component with the period of 24 hr corresponds to the migrating diurnal tide (hereafter DW1). Similarly, the W2 and W3 components with the periods of 12 and 8 hr correspond, respectively, to the migrating semidiurnal tide (SW2) and migrating terdiurnal tide (TW3).

In both hemispheres, the amplitudes of DW1, SW2, and TW3 are above the 95% confidence level. In the Northern Hemisphere, the mean amplitude and its corresponding standard deviation of DW1, SW2, and TW3 are 52.7 ± 9.2 , 26.6 ± 4.7 , and 9.3 ± 1.9 kA, respectively. In the Southern Hemisphere, they are 16.7 ± 6.4 , 14.7 ± 4.7 , and 7.1 ± 1.9 kA. The larger amplitude in the Northern Hemisphere can be attributed to the higher ionospheric conductivities. Besides, it is possible that there is north-south asymmetry in tidal forcing. For instance, Zhang and Shepherd (2005) analyzed the monthly behavior of the diurnal tide in the thermospheric wind from 1992 to 1996 for latitudes between 40°S and 40°N . They noted that the monthly diurnal tide is consistently higher in the Northern Hemisphere than in the Southern Hemisphere during equinoxes between altitudes of 100 and 110 km, aligning with our findings.

It is not surprising to find migrating tidal components (DW1, SW2, and TW3) in the Sq current system since ionospheric conductivities in the E-region are strongly controlled by solar radiation. During day, ionospheric conductivities increase, while they decrease at night, leading to migrating tidal variations in Sq currents. However, the northern and southern Sq current intensities show very weak correlation (i.e., $r = 0.05$ for DW1, $r = 0.17$ for SW2, and $r = 0.33$ for TW3). The difference in the temporal variabilities of DW1, SW2, and TW3 between the Northern and Southern Hemispheres cannot be explained by changes in solar radiation, which would affect northern and southern Sq current intensities in the same manner. It is likely that neutral winds are responsible for different temporal variations of DW1, SW2, and TW3 between the two hemispheres. Day-to-day variations of tides at E-region heights are not correlated between the Northern and Southern Hemispheres (e.g., Yamazaki et al., 2014).

While exploring the Fourier-wavelet spectral amplitude of the northern Sq current intensity across different wave numbers, we did not find any significant trend (≤ 0.1 kA/day) during May 2020, despite a positive trend observed in the northern Sq current intensity in Figure 4a. In contrast, our analysis of the southern Sq current intensity revealed a negative trend of -0.66 kA/day (or a reduction of 20.5 kA) for DW1, -0.45 kA/day (or a reduction of

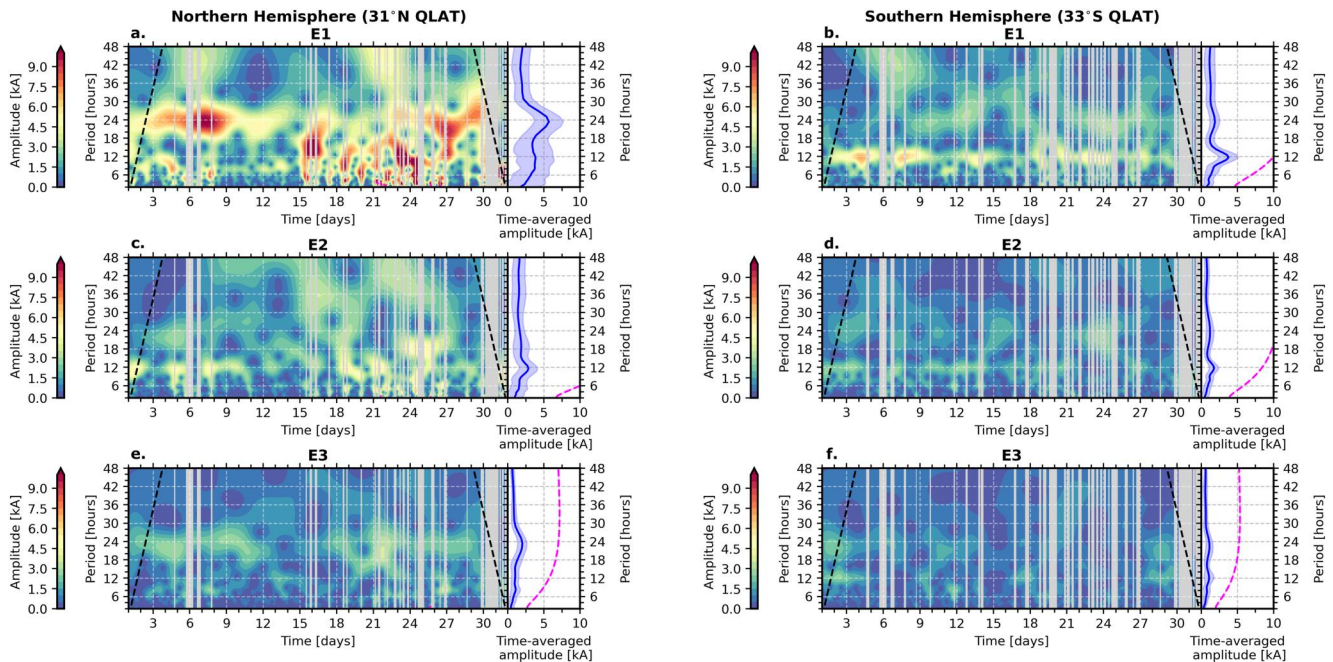


Figure 7. Same as Figure 6, except for the eastward-propagating wave component.

13.9 kA) for SW2, and -0.15 kA (or a reduction of 4.6 kA) for TW3. This may be related to the negative trend in the southern Sq current intensity affecting the amplitude reduction observed in DW1, SW2, and TW3 components.

Figure 7 is the same as Figure 6 but for the eastward-propagating components with zonal wavenumbers 1, 2, and 3 (E1, E2, and E3, respectively). For the E1 component, the mean amplitude and its corresponding standard deviation is 5.7 ± 2.0 kA at the period of 24 hr (DE1) in the Northern Hemisphere and 3.8 ± 1.4 kA at 12 hr (SE1) in the Southern Hemisphere. For the E2 component, the mean amplitude and its corresponding standard deviation are 2.8 ± 1.3 and 1.7 ± 0.6 kA in the Northern and Southern Hemispheres, respectively. Both are at the period of 12 hr (SE2). For the E3 component, the mean amplitude and its corresponding standard deviation are 2.0 ± 0.6 and 1.1 ± 0.5 kA in the Northern and Southern Hemispheres, respectively. They are not necessarily related to tides, as their wave periods are not at 24, 12, or 8 hr. The tidal amplitudes in E1, E2, and E3 are generally greater in the Northern Hemisphere than in the Southern Hemisphere, reflecting the higher ionospheric conductivities in the Northern Hemisphere. No eastward-propagating tidal components exceeded the 95% confidence threshold.

Furthermore, our investigation revealed strong day-to-day variability in the amplitude of non-migrating tidal components identified in Sq current intensities in both hemispheres. Earlier studies revealed day-to-day variability of both migrating and non-migrating tides in the dynamo region (e.g., Akmaev et al., 2008; Forbes et al., 2019; Pedatella et al., 2012).

Figure 8 presents global spectra (i.e., time-averaged spectra) for the Sq current intensities at the Northern and Southern Sq focus latitudes during 1–31 May 2020. In both hemispheres, the migrating tidal components (DW1, SW2, and TW3) are identified as dominant features with their amplitudes exceeding the 95% confidence level. Apart from migrating tidal components, some non-migrating tidal components are also visible. The eastward-propagating diurnal and semidiurnal tides with zonal wavenumber 1 (i.e., DE1 and SE1) are the largest non-migrating tidal components. Although previous studies found DE1 and SE1 in the lower thermosphere (e.g., Forbes et al., 2008; Oberheide et al., 2006), their amplitudes are relatively small compared with other non-migrating tides. Also, studies on tidal effects on the EEJ (Lühr & Manoj, 2013; Soares et al., 2022) did not find strong signatures of DE1 and SE1 in the EEJ. The mechanism for generating DE1 and SE1 in Sq currents is unclear.

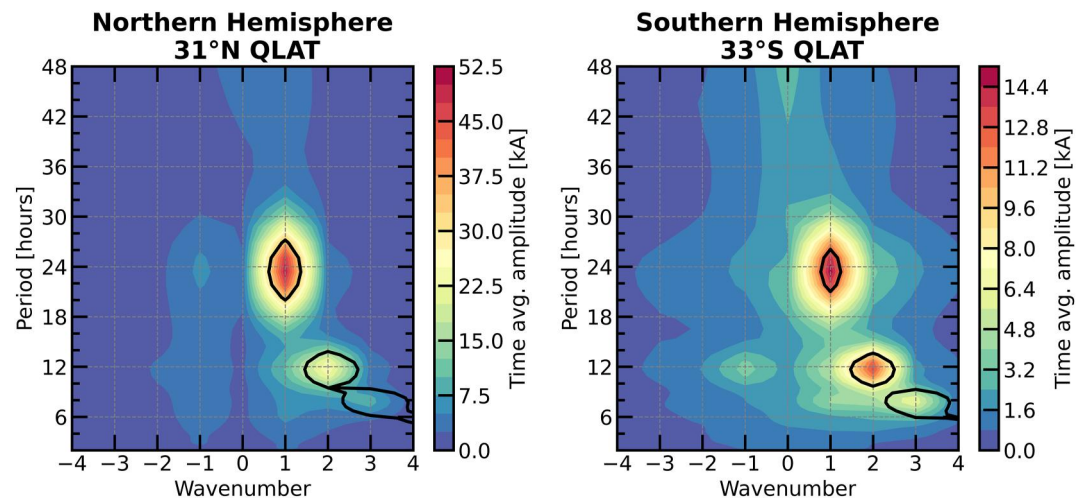


Figure 8. The contour plots illustrating the Fourier-wavelet spectra of time-averaged amplitude for the solar quiet (Sq) current intensities on 1–31 May 2020 over 31°N (left panel) and 33°S (right panel) quasi-dipole latitudes. The wavenumber >0 corresponds to the westward-propagating component and the wavenumber <0 is the eastward-propagating component. The black contour lines correspond to amplitude spectra above the 95% confidence for a red noise background.

4. Concluding Remarks

In this study, we conducted a SHA on the solar quiet daily variation of the geomagnetic field to derive the external equivalent Sq current system for each UT hour throughout 1–31 May 2020. Our focus was on examining the spatial and temporal characteristics of the Sq currents and the tidal variations in these currents in both the Northern and Southern Hemispheres. The key findings and highlights of the analysis are summarized as follows:

1. Sq currents are stronger in the Northern Hemisphere. The mean value of the Sq current intensity and its corresponding standard deviation are 145 ± 32 kA in the Northern Hemisphere and 84 ± 24 kA in the Southern Hemisphere. The stronger Sq currents in the Northern Hemisphere can be attributed to higher ionospheric conductivities during May, and are consistent with previous reports.
2. The Sq focus magnetic latitude position shows strong day-to-day variability. The mean value of the Sq focus latitude and its corresponding standard deviation are $31^\circ \pm 5^\circ$ QLAT in the Northern Hemisphere and $-33^\circ \pm 7^\circ$ QLAT in the Southern Hemisphere.
3. Spatial (longitudinal) and temporal (hour-to-hour and day-to-day) variations of the Sq current intensity are identified. The variations are not correlated between the Northern and Southern Hemispheres.
4. The wave analysis of the Sq current intensity reveals that migrating tidal components (DW1, SW2, and TW3) are predominant in both hemispheres. Their variations are not correlated between the Northern and Southern Hemispheres, indicating the contributions not only from global processes like the solar radiation effect on ionospheric conductivities but also from local wind-dynamo effects.
5. Non-migrating tidal components have also been found in Sq current intensities, among which eastward-propagating components with zonal wavenumber 1 (DE1 and SE1) are the strongest. The mechanism for the DE1 and SE1 components of Sq remains to be identified.
6. In conclusion, our analysis contributes to a better understanding of the spatiotemporal variability in the global ionospheric current system, emphasizing the presence of both migrating and non-migrating tidal wave components.

Data Availability Statement

The ground-based geomagnetic field data are available in SuperMAG (<https://supermag.jhuapl.edu/>), INTERMAGNET (<https://intermagnet.github.io/>), Embrace MagNet (<https://www.2.inpe.br/climaespacial/portal/pt/>), and LISN/IGP (<http://lisn.igp.gov.pe/jdata/database/>). The code for running the IGRF-13 model is available at

NOAA (<https://www.ngdc.noaa.gov/IAGA/vmod/igrf.html>). The code for running the CHAOS-7 model is available at DTU Space (<http://www.spacecenter.dk/files/magnetic-models/CHAOS-7/>). The hourly geomagnetic activity index Hp60 is available at GFZ Potsdam (<https://kp.gfz-potsdam.de/hp30-hp60>).

Acknowledgments

I am grateful to the Leibniz Institute of Atmospheric Physics at the University of Rostock (IAP) and their staff for their hospitality while I was a Visiting PhD student performing this work at the institute. In addition, the authors thank SuperMAG, INTERMAGNET, Embrace MagNet, and LISN/IGP for providing ground-based magnetometer data used in our analysis. Additionally, we are thankful for the accessibility of the IGRF-13 model code from NOAA and the CHAOS-7 model code from DTU Space, as well as the hourly geomagnetic activity index Hp60 data from GFZ Potsdam. SSC thanks to CAPES/MEC (Grants 88887.362982/2019-00 and 88887.694874/2022-00) and CNPq/MCTI (Grants 317449/2023-0, 300238/2024-0, and 301449/2024-4). CMD thanks to CNPq/MCTI (Grant 302675/2021-3). LCAR thanks the China-Brazil Joint Laboratory for Space Weather (CBJLSW), National Space Science Center (NSSC), Chinese Academy of Sciences (CAS) for supporting her Postdoctoral fellowship. We thank the Brazilian Ministry of Science, Technology, and Innovations (MCTI) and the Brazilian Space Agency (AEB). This study was financed in part by the Coordenação de Aperfeiçoamento de Pessoal de Nível Superior—Brasil (CAPES)—Finance Code 001.

References

- Akmaev, R. A., Fuller-Rowell, T. J., Wu, F., Forbes, J. M., Zhang, X., Anghel, A. F., et al. (2008). Tidal variability in the lower thermosphere: Comparison of Whole Atmosphere Model (WAM) simulations with observations from TIMED. *Geophysical Research Letters*, *35*(3), L03810. <https://doi.org/10.1029/2007GL032584>
- Alken, P., Thébaud, E., Beggan, C. D., Amit, H., Aubert, J., Baerenzung, J., et al. (2021). International Geomagnetic Reference Field: The thirteenth generation. *Earth Planets and Space*, *73*(1), 1–25. <https://doi.org/10.1186/s40623-020-01288-x>
- Blanc, M., & Richmond, A. D. (1980). The ionospheric disturbance dynamo. *Journal of Geophysical Research*, *85*(A4), 1669–1686. <https://doi.org/10.1029/JA085iA04p01669>
- Campbell, W. H., & Schiffmacher, E. R. (1985). Quiet ionospheric currents of the northern hemisphere derived from geomagnetic field records. *Journal of Geophysical Research*, *90*(A7), 6475–6486. <https://doi.org/10.1029/JA090iA07P06475>
- Campbell, W. H., & Schiffmacher, E. R. (1988). Quiet ionospheric currents of the southern hemisphere derived from geomagnetic records. *Journal of Geophysical Research*, *93*(A2), 933–944. <https://doi.org/10.1029/JA093iA02P00933>
- Chapman, S., & Bartels, J. (1940a). *Geomagnetism: Geomagnetic and related phenomena* (Vol. 1). Oxford University Press.
- Chapman, S., & Bartels, J. (1940b). *Geomagnetism: Analysis of the data and physical theories* (Vol. 2). Oxford University Press.
- Chulliat, A., Vigneron, P., & Hulot, G. (2016). First results from the Swarm Dedicated ionospheric field inversion chain. *Earth Planets and Space*, *68*(1), 521–545. <https://doi.org/10.1186/s40623-016-0481-6>
- Denardini, C. M., Chen, S. S., Resende, L. C. A., Moro, J., Bilibio, A. V., Fagundes, P. R., et al. (2018). The Embrace Magnetometer Network for South America: Network description and its qualification. *Radio Science*, *53*(3), 288–302. <https://doi.org/10.1002/2017RS006477>
- Doumouya, V., Cohen, Y., Arora, B., & Yumoto, K. (2003). Local time and longitude dependence of the equatorial electrojet magnetic effects. *Journal of Atmospheric and Solar-Terrestrial Physics*, *65*(14–15), 1265–1282. <https://doi.org/10.1016/j.jastp.2003.08.014>
- Emmert, J. T., Richmond, A. D., & Drob, D. P. (2010). A computationally compact representation of Magnetic-Apex and Quasi-Dipole coordinates with smooth base vectors. *Journal of Geophysical Research*, *115*(A8), A08322. <https://doi.org/10.1029/2010JA015326>
- Finlay, C. C., Kloss, C., Olsen, N., Hammer, M. D., Tøffner-Clausen, L., Grayver, A., & Kuvshinov, A. (2020). The CHAOS-7 geomagnetic field model and observed changes in the South Atlantic Anomaly. *Earth Planets and Space*, *72*(1), 156. <https://doi.org/10.1186/s40623-020-01252-9>
- Forbes, J. M., & Lindzen, R. (1976). Atmospheric solar tides and their electrodynamic effects—I. The global Sq current system. *Journal of Atmospheric and Terrestrial Physics*, *38*(9–10), 897–910. [https://doi.org/10.1016/0021-9169\(76\)90073-8](https://doi.org/10.1016/0021-9169(76)90073-8)
- Forbes, J. M., Maute, A., & Zhang, X. (2019). The nature and origins of the day-to-day variability in Earth’s surface magnetic field. *Advances in Space Research*, *64*(10), 2012–2025. <https://doi.org/10.1016/j.asr.2019.05.045>
- Forbes, J. M., Zhang, X., Palo, S., Russell, J., Mertens, C. J., & Mlynczak, M. (2008). Tidal variability in the ionospheric dynamo region. *Journal of Geophysical Research*, *113*(A2), A02310. <https://doi.org/10.1029/2007JA012737>
- Frigo, M., & Johnson, S. (1998). FFTW: An adaptive software architecture for the FFT. In *Proceedings of the 1998 IEEE International Conference on Acoustics, Speech and Signal Processing, ICASSP '98 (Cat. No. 98CH36181)* (Vol. 3, pp. 1381–1384). <https://doi.org/10.1109/ICASSP.1998.681704>
- Gjerloev, J. W. (2012). The SuperMAG data processing technique. *Journal of Geophysical Research*, *117*(A9), 9213. <https://doi.org/10.1029/2012JA017683>
- Hasegawa, M. (1960). On the position of the focus of the geomagnetic Sq current system. *Journal of Geophysical Research*, *65*(5), 1437–1447. <https://doi.org/10.1029/JZ065i005p01437>
- Hibberd, F. H., & Davidson, R. E. (1988). Global scale of the day-to-day variability of Sq. *Geophysical Journal International*, *92*(2), 315–321. <https://doi.org/10.1111/j.1365-246X.1988.tb01142.x>
- Kane, R. P. (1974). Relation between the strength of the Sq current system and its focus position. *Proceedings of the Indian Academy of Sciences Section A*, *80*(1), 17–25. <https://doi.org/10.1007/BF03046669>
- Kawano-Sasaki, K., & Miyahara, S. (2008). A study on three-dimensional structures of the ionospheric dynamo currents induced by the neutral winds simulated by the Kyushu-GCM. *Journal of Atmospheric and Solar-Terrestrial Physics*, *70*(11–12), 1549–1562. <https://doi.org/10.1016/j.jastp.2008.05.004>
- Laundal, K. M., Finlay, C. C., Olsen, N., & Reistad, J. P. (2018). Solar wind and seasonal influence on ionospheric currents from Swarm and CHAMP measurements. *Journal of Geophysical Research: Space Physics*, *123*(5), 4402–4429. <https://doi.org/10.1029/2018JA025387>
- Le Huy, M., & Amory-Mazaudier, C. (2008). Planetary magnetic signature of the storm wind disturbance dynamo currents: Ddyn. *Journal of Geophysical Research*, *113*(A2), 1–7. <https://doi.org/10.1029/2007JA012686>
- Liu, X., Han, P., Hattori, K., Chen, H., Chen, J., Jiao, L., et al. (2024). Seasonal variations of Sq current system in different longitudinal sectors and solar activities. *Journal of Geophysical Research: Space Physics*, *129*(1), e2023JA031956. <https://doi.org/10.1029/2023JA031956>
- Liu, X., Han, P., Hattori, K., Chen, H., Yoshino, C., Zhao, X., et al. (2021). Seasonal variation characteristics of geomagnetic Sq external and internal equivalent current systems in East-Asia and Oceania regions. *Journal of Geophysical Research: Space Physics*, *126*(3), e2021JA029113. <https://doi.org/10.1029/2021JA029113>
- Love, J. J. (2008). Magnetic monitoring of Earth and space. *Physics Today*, *61*(2), 31–37. <https://doi.org/10.1063/1.2883907>
- Lühr, H., & Manoj, C. (2013). The complete spectrum of the equatorial electrojet related to solar tides: CHAMP observations. *Annales Geophysicae*, *31*(8), 1315–1331. <https://doi.org/10.5194/ANGE0-31-1315-2013>
- Lühr, H., Xiong, C., Olsen, N., & Le, G. (2017). Near-Earth magnetic field effects of large-scale magnetospheric currents. *Space Science Reviews*, *206*(1–4), 521–545. <https://doi.org/10.1007/s11214-016-0267-y>
- Maeda, K., & Kato, S. (1966). Electrodynamics of the ionosphere. *Space Science Reviews*, *5*(1), 57–79. <https://doi.org/10.1007/BF00179215>
- Matzka, J., Stolle, C., Yamazaki, Y., Bronkalla, O., & Morschhauser, A. (2021). The geomagnetic Kp index and derived indices of geomagnetic activity. *Space Weather*, *19*(5), e2020SW002641. <https://doi.org/10.1029/2020SW002641>
- Oberheide, J., Forbes, J. M., Zhang, X., & Bruinsma, S. L. (2011). Climatology of upward propagating diurnal and semidiurnal tides in the thermosphere. *Journal of Geophysical Research*, *116*(A11), A11306. <https://doi.org/10.1029/2011JA016784>

- Oberheide, J., Wu, Q., Killeen, T. L., Hagan, M. E., & Roble, R. G. (2006). Diurnal nonmigrating tides from TIMED Doppler Interferometer wind data: Monthly climatologies and seasonal variations. *Journal of Geophysical Research*, *111*(A10), 679. <https://doi.org/10.1029/2005JA011491>
- Olsen, N., Lühr, H., Sabaka, T. J., Manda, M., Rother, M., Tøffner-Clausen, L., & Choi, S. (2006). CHAOS—A model of the Earth's magnetic field derived from CHAMP, Ørsted, and SAC-C magnetic satellite data. *Geophysical Journal International*, *166*(1), 67–75. <https://doi.org/10.1111/j.1365-246X.2006.02959.x>
- Owolabi, C., Ruan, H., Yamazaki, Y., Kaka, R. O., Akinola, O. O., & Yoshikawa, A. (2022). Ionospheric current variations by empirical orthogonal function analysis: Solar activity dependence and longitudinal differences. *Journal of Geophysical Research: Space Physics*, *127*(1), e2021JA029903. <https://doi.org/10.1029/2021ja029903>
- Pedatella, N. M., Forbes, J. M., & Richmond, A. D. (2011). Seasonal and longitudinal variations of the solar quiet (Sq) current system during solar minimum determined by CHAMP satellite magnetic field observations. *Journal of Geophysical Research*, *116*(A4), 4317. <https://doi.org/10.1029/2010JA016289>
- Pedatella, N. M., Liu, H. L., & Hagan, M. E. (2012). Day-to-day migrating and nonmigrating tidal variability due to the six-day planetary wave. *Journal of Geophysical Research*, *117*(A6), A06301. <https://doi.org/10.1029/2012JA017581>
- Pfaff, R., Larsen, M., Abe, T., Habu, H., Clemmons, J., Freudenreich, H., et al. (2020). Daytime dynamo electrodynamics with spiral currents driven by strong winds revealed by vapor trails and sounding rocket probes. *Geophysical Research Letters*, *47*(15), e2020GL088803. <https://doi.org/10.1029/2020GL088803>
- Rastogi, R. G. (1989). The equatorial electrojet: Magnetic and ionospheric effects. In J. Jacobs (Ed.), *Geomagnetism* (Vol. 3, pp. 461–525). Academic Press.
- Richmond, A. D. (1979). Ionospheric wind dynamo theory: A review. *Journal of Geomagnetism and Geoelectricity*, *31*(3), 287–310. <https://doi.org/10.5636/JGG.31.287>
- Richmond, A. D., Matsushita, S., & Tarpley, J. D. (1976). On the production mechanism of electric currents and fields in the ionosphere. *Journal of Geophysical Research*, *81*(4), 547–555. <https://doi.org/10.1029/JA081i004p00547>
- Rigoti, A., Chamalaun, F. H., Trivedi, N. B., & Padilha, A. L. (1999). Characteristics of the equatorial electrojet determined from an array of magnetometers in N-NE Brazil. *Earth Planets and Space*, *51*(2), 115–128. <https://doi.org/10.1186/bf03352216>
- Rishbeth, H. (1997). The ionospheric E-layer and F-layer dynamos—A tutorial review. *Journal of Atmospheric and Solar-Terrestrial Physics*, *59*(15), 1873–1880. [https://doi.org/10.1016/S1364-6826\(97\)00005-9](https://doi.org/10.1016/S1364-6826(97)00005-9)
- Soares, G., Yamazaki, Y., Morschhauser, A., Matzka, J., Pinheiro, K. J., Stolle, C., et al. (2022). Using principal component analysis of satellite and ground magnetic data to model the equatorial electrojet and derive its tidal composition. *Journal of Geophysical Research: Space Physics*, *127*(9), e2022JA030691. <https://doi.org/10.1029/2022JA030691>
- Stening, R. J. (1971). Longitude and seasonal variations of the Sq current system. *Radio Science*, *6*(2), 133–137. <https://doi.org/10.1029/RS006i002p00133>
- Stening, R. J. (1977). Ionospheric dynamo calculations with semidiurnal winds. *Planetary and Space Science*, *25*(11), 1075–1080. [https://doi.org/10.1016/0032-0633\(77\)90154-4](https://doi.org/10.1016/0032-0633(77)90154-4)
- Stening, R. J., Reztsova, T., & Minh, L. H. (2005). Day-to-day changes in the latitudes of the foci of the Sq current system and their relation to equatorial electrojet strength. *Journal of Geophysical Research*, *110*(A10), 1375. <https://doi.org/10.1029/2005JA011219>
- Stening, R. J., & Winch, D. E. (2013). The ionospheric Sq current system obtained by spherical harmonic analysis. *Journal of Geophysical Research: Space Physics*, *118*(3), 1288–1297. <https://doi.org/10.1002/JGRA.50194>
- Suzuki, A. (1978). Geomagnetic Sq field at successive Universal Times. *Journal of Atmospheric and Terrestrial Physics*, *40*(4), 449–463. [https://doi.org/10.1016/0021-9169\(78\)90177-0](https://doi.org/10.1016/0021-9169(78)90177-0)
- Takeda, M. (1999). Time variation of global geomagnetic Sq field in 1964 and 1980. *Journal of Atmospheric and Solar-Terrestrial Physics*, *61*(10), 765–774. [https://doi.org/10.1016/S1364-6826\(99\)00028-0](https://doi.org/10.1016/S1364-6826(99)00028-0)
- Takeda, M. (2002). Features of global geomagnetic Sq field from 1980 to 1990. *Journal of Geophysical Research*, *107*(A9), 1252. <https://doi.org/10.1029/2001JA009210>
- Takeda, M., & Maeda, H. (1980). Three-dimensional structure of ionospheric currents 1. Currents caused by diurnal tidal winds. *Journal of Geophysical Research*, *85*(A12), 6895–6899. <https://doi.org/10.1029/JA085iA12p06895>
- Tarpley, J. D. (1970). The ionospheric wind dynamo—II: Solar tides. *Planetary and Space Science*, *18*(7), 1091–1103. [https://doi.org/10.1016/0032-0633\(70\)90110-8](https://doi.org/10.1016/0032-0633(70)90110-8)
- Torrence, C., & Compo, G. P. (1998). A practical guide to wavelet analysis. *Bulletin of the American Meteorological Society*, *79*(1), 61–78. [https://doi.org/10.1175/1520-0477\(1998\)079<0061:APGTWA>2.0.CO;2](https://doi.org/10.1175/1520-0477(1998)079<0061:APGTWA>2.0.CO;2)
- Truskowski, A. O., Forbes, J. M., Zhang, X., & Palo, S. E. (2014). New perspectives on thermosphere tides: 1. Lower thermosphere spectra and seasonal-latitude structures. *Earth Planets and Space*, *66*, 1–17. <https://doi.org/10.1186/s40623-014-0136-4>
- Valladares, C. E., & Chau, J. L. (2012). The Low-Latitude Ionosphere Sensor Network: Initial results. *Radio Science*, *47*(4), RS0L07. <https://doi.org/10.1029/2011RS004978>
- Winch, D. E. (1981). Spherical harmonic analysis of geomagnetic tides, 1964–1965. *Philosophical Transactions of the Royal Society of London Series A: Mathematical and Physical Sciences*, *303*(1473), 1–104. <https://doi.org/10.1098/RSTA.1981.0193>
- Yamazaki, Y. (2022). Solar and lunar daily geomagnetic variations and their equivalent current systems observed by Swarm. *Earth Planets and Space*, *74*, 1–21. <https://doi.org/10.1186/S40623-022-01656-9>
- Yamazaki, Y. (2023). A method to derive Fourier-wavelet spectra for the characterization of global-scale waves in the mesosphere and lower thermosphere and its MATLAB and Python software (fourierwavelet v1.1). *Geoscientific Model Development*, *16*, 4749–4766. <https://doi.org/10.5194/GMD-16-4749-2023>
- Yamazaki, Y., Harding, B. J., Qiu, L., Stolle, C., Siddiqui, T. A., Miyoshi, Y., et al. (2023). Monthly climatologies of zonal-mean and tidal winds in the thermosphere as observed by ICON/MIGHTI during April 2020–March 2022. *Earth and Space Science*, *10*(6), e2023EA002962. <https://doi.org/10.1029/2023ea002962>
- Yamazaki, Y., Häusler, K., & Wild, J. A. (2016). Day-to-day variability of midlatitude ionospheric currents due to magnetospheric and lower atmospheric forcing. *Journal of Geophysical Research: Space Physics*, *121*(7), 7067–7086. <https://doi.org/10.1002/2016JA022817>
- Yamazaki, Y., Matzka, J., Stolle, C., Kervalishvili, G., Rauberg, J., Bronkalla, O., et al. (2022). Geomagnetic activity index H_{po}. *Geophysical Research Letters*, *49*(10), e2022GL098860. <https://doi.org/10.1029/2022GL098860>
- Yamazaki, Y., & Maute, A. (2017). Sq and EEJ—A review on the daily variation of the geomagnetic field caused by ionospheric dynamo currents. *Space Science Reviews*, *206*(1–4), 299–405. <https://doi.org/10.1007/s11214-016-0282-z>
- Yamazaki, Y., Richmond, A. D., Maute, A., Liu, H. L., Pedatella, N., & Sassi, F. (2014). On the day-to-day variation of the equatorial electrojet during quiet periods. *Journal of Geophysical Research: Space Physics*, *119*(8), 6966–6980. <https://doi.org/10.1002/2014JA020243>

- Yamazaki, Y., Yumoto, K., Cardinal, M. G., Fraser, B. J., Hattori, P., Kakinami, Y., et al. (2011). An empirical model of the quiet daily geomagnetic field variation. *Journal of Geophysical Research*, *116*(A10), 19113. <https://doi.org/10.1029/2011JA016487>
- Yamazaki, Y., Yumoto, K., Uozumi, T., & Cardinal, M. G. (2011). Intensity variations of the equivalent Sq current system along the 210° magnetic meridian. *Journal of Geophysical Research*, *116*(A10), 19595. <https://doi.org/10.1029/2011JA016632>
- Zhang, S. P., & Shepherd, G. G. (2005). Variations of the mean winds and diurnal tides in the mesosphere and lower thermosphere observed by WINDII from 1992 to 1996. *Geophysical Research Letters*, *32*(14), 1–4. <https://doi.org/10.1029/2005GL023293>